Research Article

QiZheng Cao, Li Fan*, HaiYan Chen*, YuRong Xu, and LiHua Dong

Corrosion behavior of WC–Co coating by plasma transferred arc on EH40 steel in low-temperature

https://doi.org/10.1515/htmp-2022-0010
received November 23, 2021; accepted December 22, 2021

Abstract: To investigate the corrosion behavior of WC–Co composite coating, plasma transferred arc (PTA) welding was applied to prepare WC–Co coating on hull steel EH40 for achieving good metallurgical bonding. The phases of coatings were mainly composed of WC particles, solid solution γ-Co, Fe_3Ni_2, SiO_2 and Mo_2C. After electrochemical test, it can be concluded that Co-based coating with 45% WC content has better corrosion resistance in low temperature marine environment for obtaining denser oxide film. Through X-ray photo electron spectroscopy (XPS) analysis, the main corrosion products of immersion were $Co(OH)_2$ and Co_3O_4. These corrosion products aggregate to form a stable corrosion product film, which plays some protective role for the coating. Hard particle WC is also partially oxidized to WO_3. The pitting hole of 60% WC is the most serious. Pitting corrosion is easy to occur at the interface defects.

Keywords: EH40 steel, low-temperature corrosion, plasma transferred arc, WC–Co composite coatings

1 Introduction

Since the 21st century, oil and gas resources and biological resources have drawn more and more attention by scientists and energy industries. According to the survey and statistics [1], the energy in the Arctic Circle accounts for 22% of the total unproved energy in the world. First of all, it is necessary to solve the problem that hull steel can adapt to extremely low-temperature seawater corrosion and the stress damage of ice to the ship plate in Arctic region. Polar icebreakers have two ice breaking methods. One is continuous ice breaking, and the other is impact ice breaking. In either case, there are fatigue corrosion and electrochemical corrosion problems in the ice breaking collision area of the bow steel of polar icebreakers [2,3]. DH and EH grades of high-strength steel for ships have excellent low-temperature toughness and strength and good welding performance [4].

Corrosion situation of hull steel without protective measures in marine environments is severe. Shen et al. [5] studied EH40 steel that was corroded in simulated marine low-temperature environment. Porous corrosion products like $Fe(Cl_xO_y)$ and Fe_3O_4 were formed on the surface of the steel, which could not protect the steel surface better and the corrosion morphology of the surface was mostly pitting corrosion. The corrosion resistance of EH40 in cold sea water was poor. Tribocorrosion on EH47 high-strength ship hull steel in 3.5 wt% NaCl solution also indicated that the corrosion product film of steel has no obvious protective effect in NaCl solution. At the same time, the interaction of the micro-voids and pits between wear and corrosion accelerates the corrosion of steel surface [6].

In order to protect the surface of steel, the protection method of Co based with hard particle tungsten carbide (WC)-reinforced composite coating has been applied maturely. The high solubility of WC in a cobalt matrix at high temperatures with excellent wetting properties are relatively superior as compared to the Ni and Fe binders. Wei et al. [7,8] studied the corrosion on WC–Co–(Ni)–(Cr) alloy. It was found that in neutral solution, WC–Co and WC–Co–(Cr) were mainly corroded by the dissolution of Co, and the corrosion products were mainly composed of $Co(OH)_2$. The dense oxide film can block the corrosion of surface pitting corrosion. Scendo and Szczerba [9] studied the effect of heat treatment on the corrosion of low carbon steel coated with WC–Co–Al_2O_3 cermet composites, the Al_2O_3 content has a significant effect on the increase in the chemical corrosion resistance of the base steel.

* **Corresponding author: Li Fan,** College of Mechanical and Electronic Engineering, Shanghai Jian Qiao University, Shanghai 201306, China, e-mail: 18126@gench.edu.cn
* **Corresponding author: HaiYan Chen,** College of Ocean Science and Engineering, Shanghai Maritime University, Shanghai, 201306, China, e-mail: hychen@shmtu.edu.cn
QiZheng Cao, YuRong Xu, LiHua Dong: College of Ocean Science and Engineering, Shanghai Maritime University, Shanghai 201306, China

Wang et al. [10] prepared WC/Co coating by HOVF, but due to the decarburization of WC during spraying, extra phase formation is detrimental to the performance of the WC–Co coating. Liu et al. [11] researched erosion-corrosion of HVOF WC–Co coating in 3.5 wt% NaCl solution, and found that due to the combined effect of corrosion and erosion, the edge of WC particles surrounded by Co binding phase generated microcracks.

Plasma transferred arc (PTA) surfacing technology uses high-energy density plasma arc as heat source. This technique is widely utilized in surface engineering for its high-power characteristics. During the melting process of PTA, a strong metallurgical bond was formed between the coating and the substrate. The columnar dendrites and interdendritic precipitates were shown in the metallographic structure [12,13]. Hard phases with different components are formed in the coating. The hardness and wear resistance of the coating were significantly improved by PTA surface modification. The main reasons for the significant improvement in the wear and corrosion properties are the newly formed hard carbide phase and the microstructure defects eliminated by the PTA surface modification.

The research works listed above all focused on the corrosion situation of WC–Co coating in 3.5 wt% NaCl solution at atmospheric temperature/high temperature. Generally, WC–Co coating has good corrosion resistance in atmospheric temperature/high temperature environment. However, only few studies have been done on coating corrosion tests at low temperature. In this work, the corrosion situation of WC–Co coating in simulated low temperature of –40°C seawater environment was studied. Effects of corrosion situation on the low-temperature corrosion behavior were studied in order to help to improve materials used for low-temperature protection of EH40 steel for icebreakers.

2 Materials and methods

2.1 Experimental materials

The high-strength low-temperature hull steel EH40 was used as the substrate material with dimensions of 100 mm × 100 mm and a thickness of 30 mm. The chemical compositions of the samples are given in Table 1. Cobalt-based alloy powder (Höganäs, Shanghai, China), with an average diameter of 124 μm, melting point of 1,300–1,495°C and specific particle size distribution as shown in Figure 1, was used in this experiment. Its compositions are shown in Table 2. The powders mixed with 0, 30, 45 and 60% mass of spheroidized WC are labeled as Co, Co + 30% WC, Co + 45% WC and Co + 60% WC, respectively.

2.2 Preparation of the PTA composite coatings

In order to prevent blocking of the powder feeding pipe and increase liquidity, the tested powders of Co + 30% WC, Co + 45% WC and Co + 60% WC are mixed in a ball mill at 100 rpm for 1 h. In this experiment, PTA composite coatings were cladded with PTA-PHE plasma welding machine (Saint-Cobain, France), with PTA parameters set to 130 A and 30 V, with feed rate of 10 g·min^{-1} and working speed of 50 mm·min^{-1}. The central gas pressure was 0.3 MPa, ion gas (Ar) flow was 0.4 m^3·h^{-1} and the

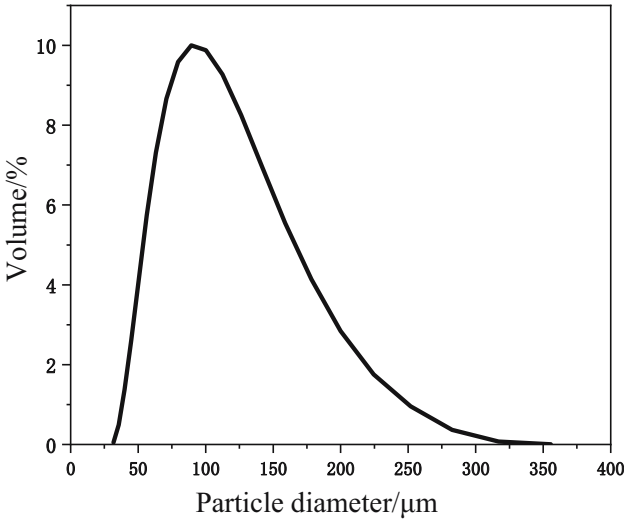

Figure 1: Particle size distribution of Co powder.

Table 1: Chemical compositions of the high strength hull steel EH40 (wt%)

Elements	P	S	C	Cr	Si	Mn	Mo	V	Ni	Cu	Fe
Content	0.010	0.0015	0.16	0.20	0.15	0.90	0.08	0.10	0.40	0.35	Bal.

Table 2: Chemical compositions of Co-based alloy powder (wt%)

Elements	Mo	W	Ni	Fe	Cr	Si	C	Co
Content	6	2.5	10	3.5	28	1	0.1	Bal.

vibration extent was 20 mm. After the PTA process, the samples were cut into two sizes 10 mm × 10 mm × 4 mm and 5 mm × 5 mm × 4 mm by wire cutting technology. PTA processing schematic representation is shown in Figure 2.

2.3 Microstructural characterization and phase composition

The coating surface condition after PTA process was analyzed using scanning electronic microscopy (SEM, JSM-7500F), X-ray diffraction (XRD; PANalytical X, Pert Pro X) and energy dispersive spectrometry (EDS; JEOL JSM7500F). The side of the coating contains 2 mm × 10 mm composite coating and 2 mm × 10 mm steel substrate. The coating surface of 10 mm × 10 mm was ground on SiC paper to 2,000 grit and polished to a mirror surface with 1.5 μm Al_2O_3. The specimens were etched using the solutions of hydrochloric acid and nitric acid with volume ratio of 3:1 for about 5 min to observe the morphology after etching. The phase composition of the composite coatings was identified by XRD with Cu-Kα radiation source (40 kV, 10 mA, scanning range of 2θ from 10° to 90°).

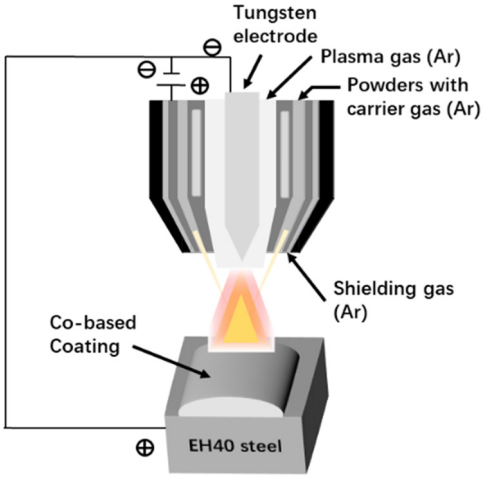

Figure 2: PTA processing schematic representation.

2.4 Low temperature immersion test and XPS analysis

Simulating the cold Arctic marine environment, the Co, Co + 30% WC, Co + 45% WC and Co + 60% WC samples of size 5 mm × 5 mm × 4 mm were, respectively, immersed in 3.5 wt% NaCl solution and 0.5 mol·L^{-1} HCl at −40°C for 240 h. The 3D non-contact white light interferometer (German BRUKER UMT TriboLab, Germany) was used to observe the surface morphology after low temperature immersion. Then, XPS test was performed by ESCALAB 250Xi surface analyzer (Thermo Fisher Scientific Company) to analyze the corrosion products after immersion with monochrome Al target (1486.6 eV).

2.5 Electrochemical corrosion test

The electrochemical tests conclude the polarization curves and electrochemical impedance spectra (EIS) were done using Electrochemical workstations (CHI600E Series Electrochemical Analyzer/Workstation, Shanghai Chenhua Instrument Co., Ltd). The electrochemical corrosion tests were performed in 3.5 wt% NaCl solution after immersed at −40°C for 240 h. A three-electrode cell was used with the samples of size 10 mm × 10 mm × 4 mm were used as working electrode (WE), a standard saturated calomel electrode (SCE) served as the reference electrode and a platinum tablet was as an auxiliary electrode. The working principle is shown in Figure 3.

Before the potentiodynamic polarization test, the samples were immersed in open circuit potential for 60 minutes to ensure steady-state conditions. The corrosion current (i_{corr}) and corrosion potential (E_{corr}) had a scan rate of 2 mV·s^{-1} and the scanning range was −1.0 V to 1.5 V. The frequency range of 10^{-2} to 10^5 Hz and the loading voltage with a voltage amplitude of 10 mV were used to conduct the EIS. ZSimpWin software to analyze

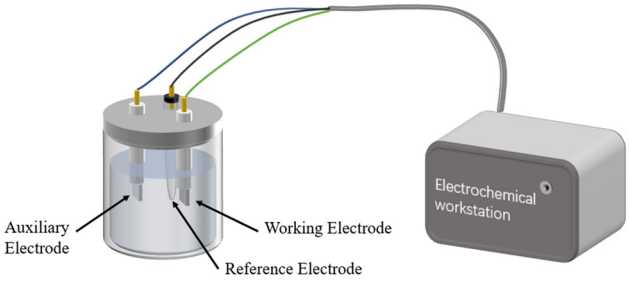

Figure 3: Schematic diagram of the electrochemical experiment.

impedance curve was installed in a computer interfaced with Chi660e software to collect the EIS data.

3 Results and discussion

3.1 Microstructure and phase analysis

X-ray diffraction patterns for pure Co coating and WC-reinforced Co-based coating samples are shown in Figure 4(a) and (b). In the XRD pattern of pure Co coating sample, γ-Co and FeNi were the major phases, with $MoNi_4$ and $Cr_2Fe_{14}C$ dispersed in the γ-(Ni, Fe) matrix. Chao et al. [14] also found that after laser cladding with nickel base alloy powder, dendrite (Cr, Fe) carbides are distributed in γ-(Ni, Fe) matrix. The alloy phase Fe_3Ni_2 show that the transitioned Ni deposition layer forms a good metallurgical bonding with the substrate, which can improve the bonding strength between the coating and the substrate to a certain extent and prevent the coating from spalling. While the phase of WC-reinforced Co-based coating samples have additional phases such as hard phase like WC, W_2C and bonding phase Mo_2C.

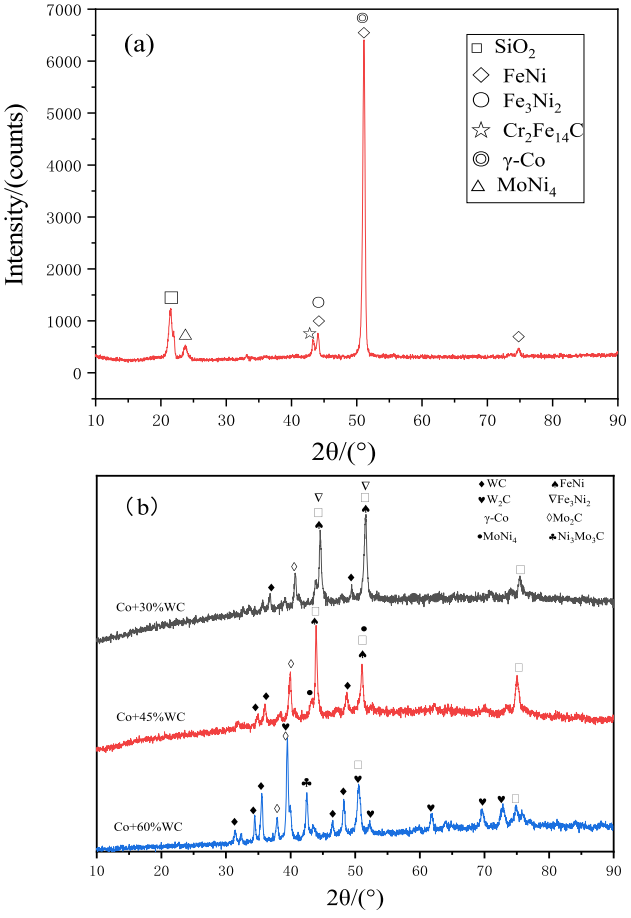

Figure 4: XRD spectra of PTA coatings. (a) Co coating; (b) Co + WC coating.

However, Fe_3Ni_2 phase hardly exists in Co + 45% WC and Co + 60% WC samples. W_2C exists in Co + 60% WC samples. In terms of thermodynamics, W_2C is considered to be a meta-stable phase. According to the equilibrium binary WC phase, WC phase decomposes into W_2C and C below 1,255°C [15]. It has been reported that thermal conductivity increases with decrease in the Co content and increase in the WC grain size [16]. Co + 60% WC sample contains the least specific gravity of Co. Because of the higher thermal conductivity, the W_2C phase appears in Co + 60% WC, the Fe_3Ni_2 phase is not easy to form in Co + 60% WC, and it is easier to form more Mo_2C phases.

Observation of the upper section of Co-based overlays with 60% WC are shown in the Figure 5(a) and (b). According to the results of XRD analysis (Figure 4(b)) of the composite coating and with reference to the results of SEM and EDS analyses, which are shown in Figure 5(c) and (d), the primary reinforcement phases containing a high concentration of W element and a sort of Si element, with the XRD reference, can be identified as W_2C, WC and SiO_2. Gray black area as shown in Figure 5(b) is the interdendritic eutectic and dendrite structures region. The result of EDS analysis indicated that the eutectic phases contained large amounts of Cr and Co, and small amount of Mo, as shown in Table 3, considering the XRD result, the component could be Mo_2C. The dendrite structures mainly contain γ-Co(fcc) [17]. The SEM micrograph of typical cross-sections of the composite coatings is shown in Figure 6.

After PTA welding, the SEM micrograph of typical cross-sections of the composite coatings is shown in Figure 6. From Figure 7(a) and (b), and according to XRD results, the dendrite is the $Cr_2Fe_{14}C$ carbide and FeNi, while the γ-Co matrix is connected to the eutectic layer [18].

It has been known that the corrosion resistance can be effectively improved by adding WC particles and forming metal matrix ceramic particles-reinforced composite coating by powder metallurgy [19–21]. By comparing the Co-based coatings with different contents of WC, Figure 7(c) and (d) shows the strengthening phase and the surrounding layered eutectic are connected with the γ-Co, the eutectic layer is structurally equivalent to a layer of transition structure. The microscopic interface structure displayed by this transition structure makes the strengthening phase and the matrix more tightly combined, and the ability to resist wear and corrosion is enhanced. In Figure 7(c), (e) and (g), there are some small

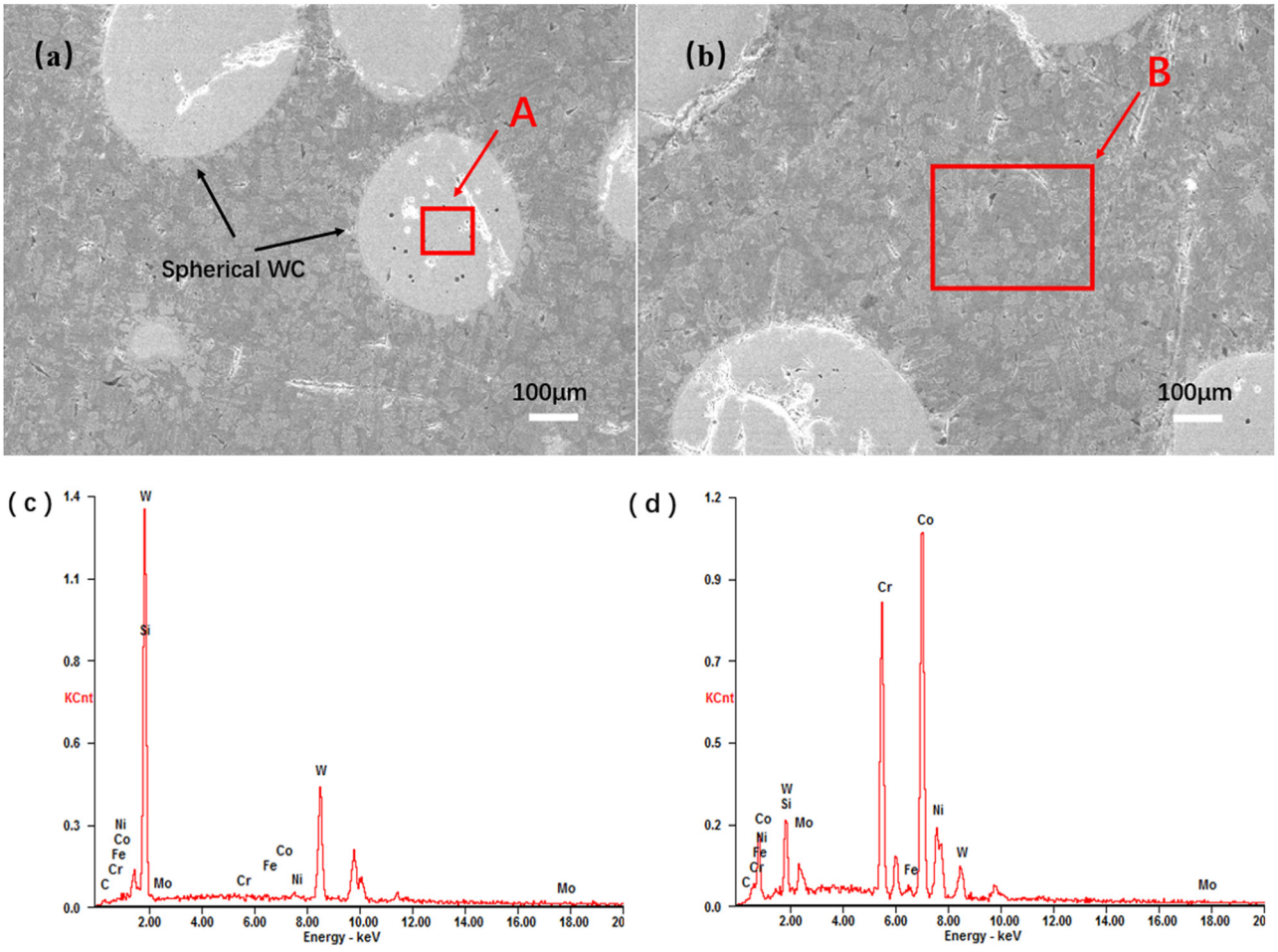

Figure 5: Microstructure of the Co + 60% WC PTA coating. (a) Spherical WC; (b) Co-based coating; (c) EDS spectrum of region A marked in (a); (d) EDS spectrum of region B marked in (b).

Table 3: Chemical compositions of the marked regions of Co + 60% WC sample (%)

Region	C	Si	Mo	Cr	Fe	Co	Ni	W
A	2.99	5.33	—	0.36	0.42	—	0.28	90.62
B	2.61	3.34	3.68	18.19	11.07	35.39	7.32	18.40

voids on the surface of the spherical WC [22]. With the increase in the WC content, the defects such as small holes in the coating tend to increase. The main reason is that the melting point of WC in PTA process is as high as 2,870°C, the melting rate of WC particles is low at high temperature, and most of the WC particles remain

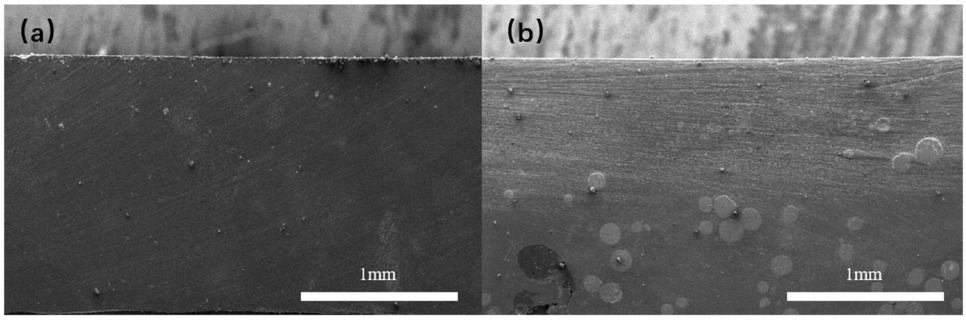

Figure 6: Microstructure of typical cross-sections of the composite coatings. (a) Co; (b) Co + 45% WC.

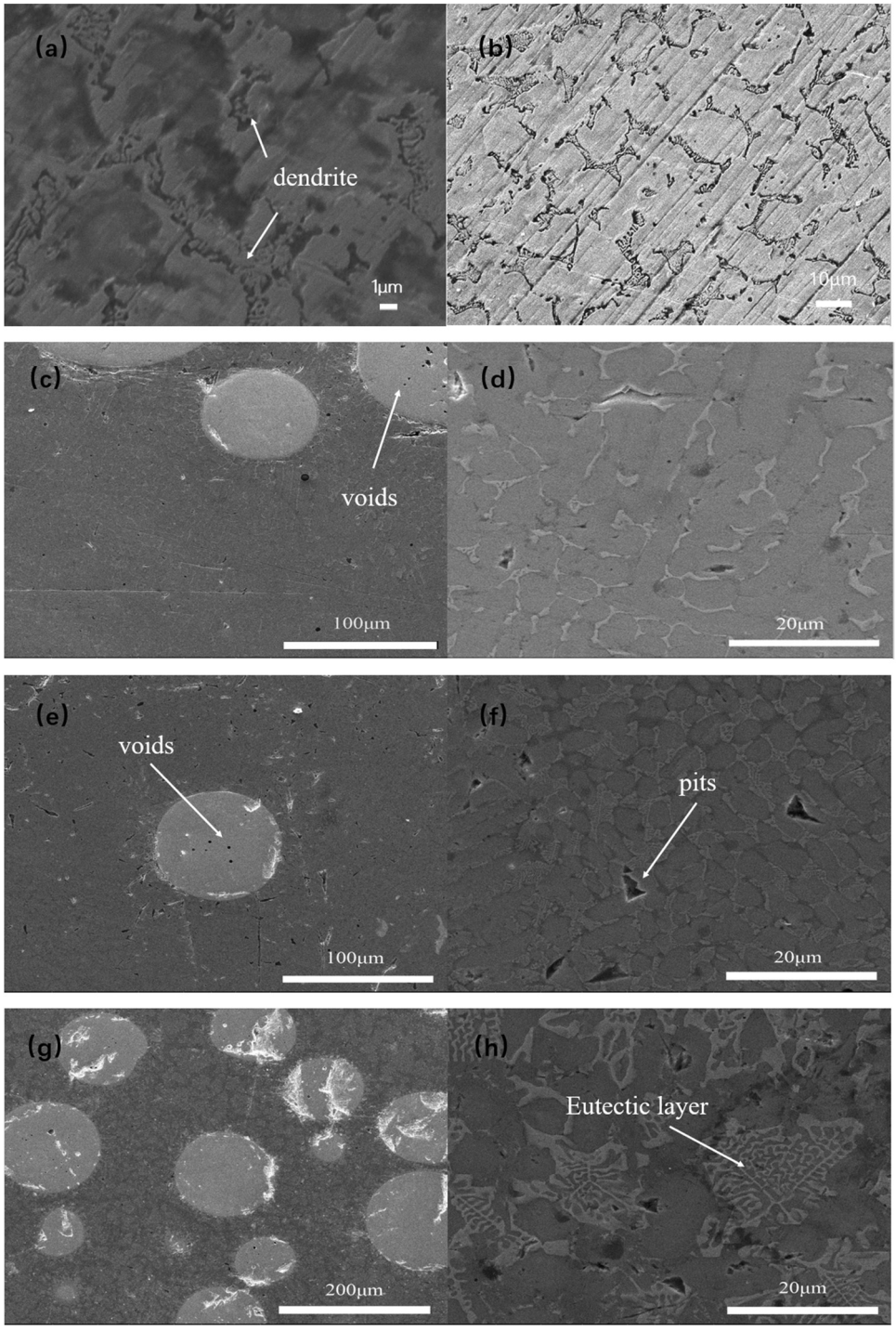

Figure 7: Microstructure of the Co-based PTA coating. (a and b) Co; (c and d) Co + 15% WC; (e and f) Co + 45% WC; (g and h) Co + 60% WC.

spherical. With the increase in the WC content, liquid Co-based alloy cannot quickly wet the whole WC surface and fill all its pores. Therefore, with the increase in the WC content, the number of small pores and other defects in the coating increases [23].

It is shown by the Figure 7(d), (f) and (h) that there are different degrees of pitting corrosion on the coating surface. Compared with 45% WC, 60% WC has more pitting holes on the surface, and 30% WC contains less hard alloy phases, so 45% WC has better corrosion resistance.

3.2 Potentiodynamic polarization results

The potentiodynamic polarization curves of the Co-based coating and several coatings with different content of Co–WC coatings are presented in Figure 8. As a whole, the anode curve remains similar, and the cathode curve moves obviously with the addition of spherical WC, this change could be due to the different extent of the cathodic reaction. The cathodic activity mainly occurs in the WC particles and forms a galvanic couple between the WC and Co phases, which affects the corrosion of the WC–Co coating [24]. However, the cathodic activity could be different due to the different amounts of WC in the coating. It can also be found that the corrosion current density of Co-based coating is greater than WC-reinforced Co-based coating in anode polarization region from 0.25 to 1 V. The cobalt binder has a lower corrosion potential compared to the WC phase, so the cobalt binder has preferential solubility, while the WC phase is protected from the cathode [25]. Therefore, the composite material has higher corrosion stability by adding WC particles [26].

Both Co + 45% WC and Co + 60% WC showed very small spontaneous passivation interval in the test after cryogenic treatment. There is a passivation film formed by metal on the coating surface. Cl^- will form soluble compounds with cations in the passivation film, destroying the self repairment and dissolution of the passivation film, resulting in the gradual disappearance and further corrosion of the passivation film, and the deepening of small hole corrosion will deepen the corrosion pits, which may be due to the high solubility of chloride ions and stronger corrosion ability in cryogenic environment. When the potential is larger than 0.76 V, the anodic current density of Co + 30% WC increases sharply, indicating that the passive film covering the composite alloy surface experiences the transpassive dissolution [27,28].

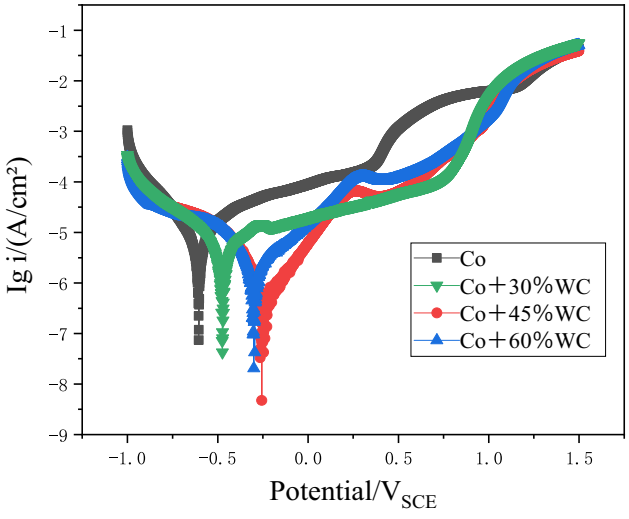

Figure 8: Potentiodynamic polarization curves of Co-WC coatings and pure Co coating in 3.5 wt% NaCl solution.

It can be seen from Figure 8 that in the anode region, the three groups of WC-reinforced Co-based coatings show obvious activation passivation transition characteristics in 3.5 wt% NaCl solution, and all show a wide passivation range, which shows their good corrosion resistance in sea water. The self-corrosion potential E_{corr}, self-corrosion current density i_{corr} and polarization resistance R_P were obtained by fitting the potentiodynamic polarization curve with the software of electrochemical workstation. The values of the cathode Tafel slope β_c and the anode Tafel slope β_a are obtained by the method of extrapolating the slope of the Tafel curve. The fitting data are shown in Table 4. It can be seen that the E_{corr} of Co + 45% WC was higher than other WC–Co composite coatings, that means adding 45% WC particles have better chemical stability and lower corrosion tendency in all the test samples.

The i_{corr} values of WC–Co coatings can be used to evaluate the corrosion rates. Comparing the four samples, the i_{corr} values have a two-fold trend increase (looking from the top to the bottom of the Table 4). The Co + 45% WC coating has the lowest i_{corr} value, from the perspective of the dynamic characteristic of the corrosion process, it can be seen that it has the best corrosion resistance. The polarization resistance (R_p) is related to the corrosion product films resistance (R_f) and charge transfer resistance (R_{ct}) [29]. From the point of view of the value change trend, the change trend of R_p is inversely proportional to i_{corr} value and the value of the coating with WC reinforced is obviously larger than that

Table 4: Corrosion parameters fitting results according to the potentiodynamic polarization curves in 3.5 wt% NaCl solution

Samples	E_{corr} (V)	i_{corr} (μA·cm^{-2})	R_p (kΩ)	β_a (mV·dec^{-1})	β_c (mV·dec^{-1})
Co + 45% WC	−0.256	0.9503	40.065	4.645	6.775
Co + 60% WC	−0.300	2.541	19.402	3.242	5.576
Co + 30% WC	−0.474	4.34	11.352	3.500	5.325
Co	−0.605	8.834	5.716	3.999	4.611

of the Co-based coating. Samples of 30% WC, 60% WC and 45% WC have a two-fold increase basically. In short, it can be concluded that Co + 45% WC coatings possessed the best corrosion resistance among the four test samples in NaCl solution after cryogenic treatment.

3.3 Electrochemical impedance spectroscopy analysis

Figure 9 shows the (a) Nyquist plots, (b) Bode impedance plots and (c) Bode angle plots test results of four groups

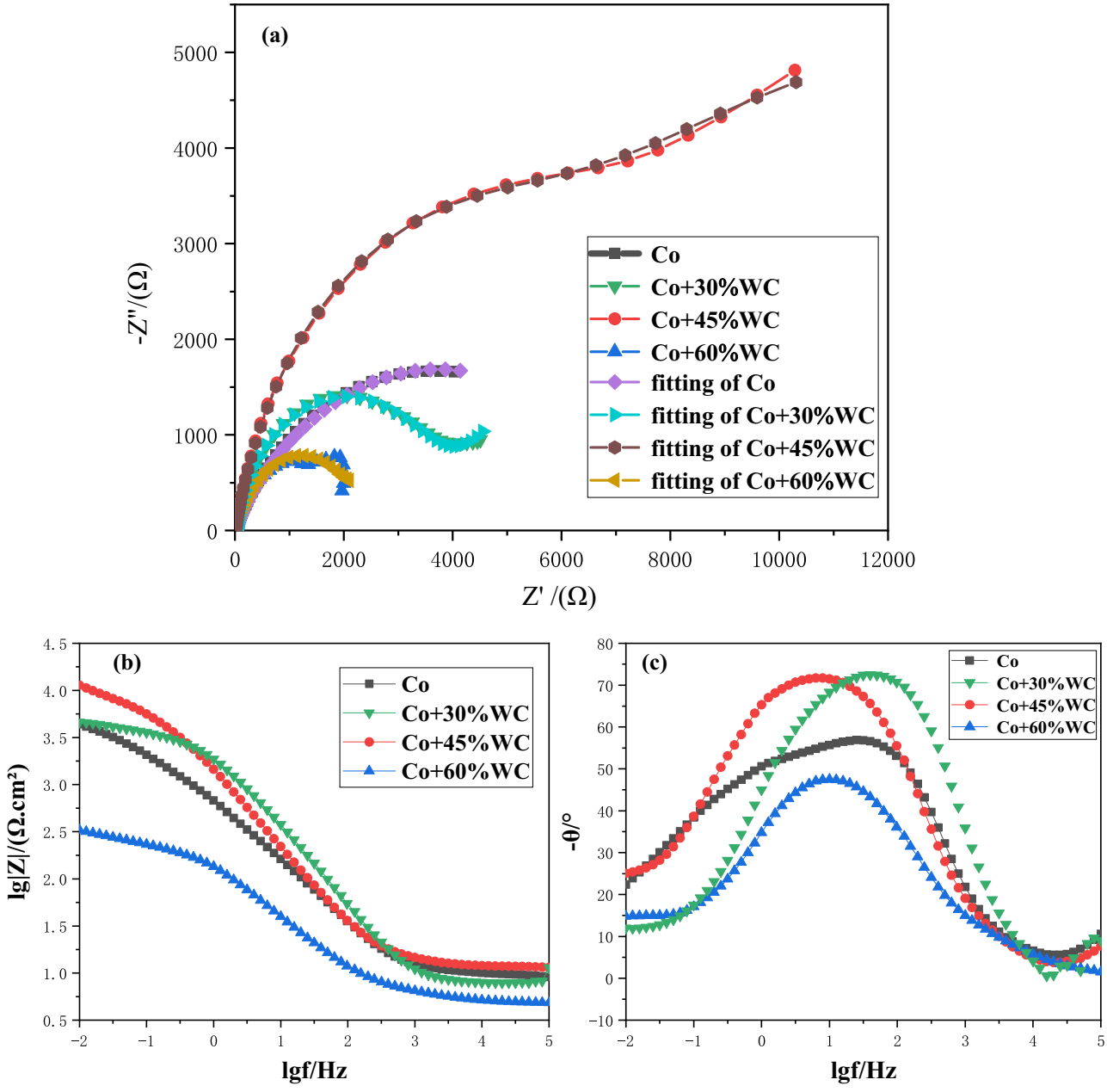

Figure 9: Impedance spectra of Co–WC coatings and Co coating in 3.5 wt% NaCl solution. (a) Nyquist plots; (b) Bode impedance plots and (c) Bode angle plots.

of samples after low temperature immersion at −40°C for 240 h in 3.5 wt% NaCl solution. As shown in Figure 9(a), the Nyquist plots of tests composite coating shows two capacitive reactance arcs. In pure Co coating, a semi-circle with capacitive reactance characteristic arc is observed in the high-frequency zone, which represents the reaction of the corrosion product layer, and the low-frequency capacitive reactance arc representing the electrode process of the metal layer appears in the low-frequency region, the high-frequency constant can show whether there is an oxide film on the surface of the coating [30,31].

While the samples of WC–Co coatings show analogous impedance characteristics, the samples have similar corrosion processes. In the high-frequency region, it is shown as a capacitive reactance arc, and in the low-frequency region, it is the low-frequency Warburg impedance representing the diffusion process. The radii of the capacitive loops arc at low frequencies reflect the corrosion resistance of the coatings. It can be seen that the radius of the capacitive arc increases gradually with the addition of WC content and then when the content is 60%, the radius of the capacitive reactance arc is reduced to the minimum.

The corresponding Bode plots are displayed in Figure 9(b) and (c). In the high frequency zone, the phase angles of the four samples are close to 0°, and the solution impedance is very small at the beginning of the reaction. In the medium frequency zone, the phase angle of Co + 45% WC and Co + 30% WC reaches the maximum θ_{max}, and compared with Nyquist plots, it can also be seen that it shows obvious capacitive reactance characteristics. The broad peak of the phase angle implied that there was more than one time constant. While in low frequency of 0.01 Hz, the values of $|Z|$ are 4,200 Ω·cm^2 (Co), 4,800 Ω·cm^2 (Co + 30% WC), 12,000 Ω·cm^2 (Co + 45% WC), 2,000 Ω·cm^2 (Co + 60% WC), respectively. It can be seen that Co + 45% WC forms a better passive film under low temperature corrosion.

Figure 10 presents the equivalent circuit of pure Co coating and WC–Co coatings. In the circuit, R_s is the resistance of the corrosion solution, Q_{dl} represents the reaction interface electric double layer capacitance. Q_f and R_f represent the capacitance and resistance of the corrosion products. R_{ct} is the charge transfer resistance. W represents the corrosion resistance formed by solution diffusion through corrosion product layer. In order to show the whole process of electrode reaction and the condition of electrode surface, ZSimpWin software is used to simulate and compare the fitting impedance data of the selected equivalent circuit models models (R(Q(R (QR)))) and (R(Q(RW(QR)))), as shown in Table 5. It was reported that in 3.5 wt% NaCl solution, with the decrease in the values of $Y_0(Q_f)$ and increase in the values of $n(Q_f)$, the porosity of the passive film would decrease, a denser oxide film can be obtained [32]. By comparing the data in Table 5, it can be found that the values of $Y_0(Q_f)$ of samples Co + 45% WC and Co + 30% WC are smaller than the other two, which means the samples of Co + 45% WC and Co + 30% WC formed relatively dense oxide film. However, the passivation region is not seen in the Co + 30% WC polarization curve, which may be because the passivation film is dissolved due to the reaction of Cl^-. The charge transfer resistance (R_{ct}) can reflect the electrochemical corrosion rate of the coating. The higher the value of R_{ct}, the better the corrosion resistance it has. Through the fitting data, it can be concluded that Co + 45% WC has the highest value compared with the other three coatings, so it is concluded that Co + 45% WC has the best corrosion resistance in cryogenic environment.

3.4 XPS analysis of low temperature immersion

XPS analysis of Co–WC coatings was obtained after immersion at −40°C for 240 h. Figure 11(a) and (b) shows the XPS full spectrum of Co + 45% WC in 3.5 wt% NaCl and

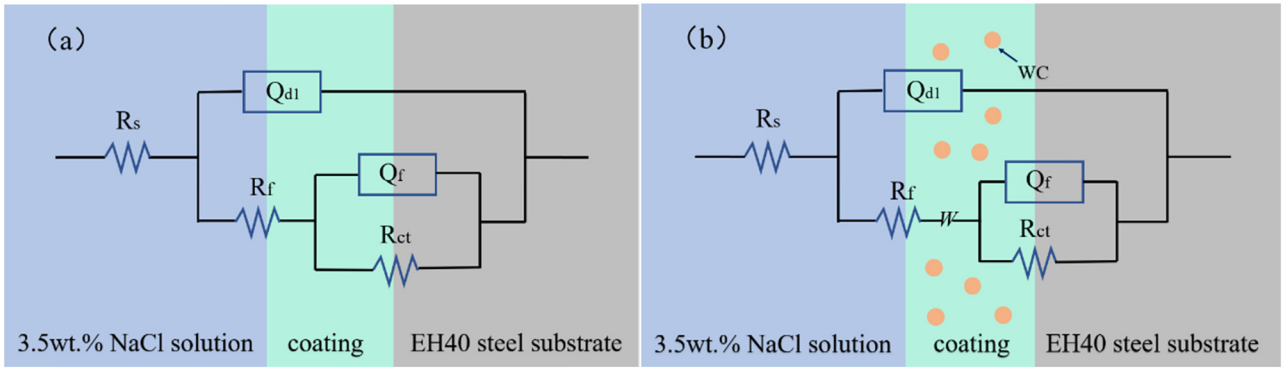

Figure 10: Equivalent circuit used for fitting impedance in 3.5 wt% NaCl solution: (a) Co coating; (b) WC–Co coatings.

Table 5: Fitting parameters obtained by ZSimpWin from the EIS data for test samples

Samples	R_s ($\Omega\cdot cm^2$)	Q_f		R_f ($\Omega\cdot cm^2$)	W	Q_{dl}		R_{ct} ($\Omega\cdot cm^2$)
		Y_0 ($\Omega^{-1}\cdot cm^{-2}\cdot sn$)	n_f			Y_0($\Omega^{-1}\cdot cm^{-2}\cdot sn$)	n_{dl}	
Co	7.032	4.228×10^{-4}	0.492	4.34	—	9.277×10^{-5}	0.85	5.011×10^{3}
Co + 30% WC	8.459	1.290×10^{-4}	1	45.22	3.401×10^{-3}	8.279×10^{-5}	0.66	3.918×10^{3}
Co + 45% WC	12.05	1.419×10^{-4}	0.838	7.439×10^{3}	7.043×10^{-4}	2.174×10^{-2}	0.79	7.690×10^{3}
Co + 60% WC	9.281	6.428×10^{-4}	0.739	2.37×10^{3}	8.416×10^{-4}	7.545×10^{-2}	1	2.192×10^{3}

0.5 mol·L^{-1} HCl solution at −40°C. It is found that the corrosion products on the surface of the sample mainly contain Ni, O, C, Cr, W and other elements, among which Ni and Cr are from Ni based alloy, C and W are from WC additive phase, and O is from corrosion products. The results show that the corrosion products are mainly Ni, Cr, W and O elements. Through the combination of the XPS full spectrum results with the narrow spectrum of test elements, the low temperature corrosion products of composite coatings could be clearly observed.

The composition of corrosion products is determined by the comprehensive strength of their XPS peaks. Figure 12(a) and (b) shows the O 1s spectrum at high resolution after low temperature immersion in two different solutions. It can be seen from the spectrum that the O 1s spectrum of both the samples is decomposed into two peaks with different binding energies, with peak values near 531.9 and 532.6, respectively. Combining with the existing literature [33], we can infer that the peak OLatt near 531.9 represents the surface lattice oxygen, such as O^{2-}. The peak near 532.6 represents the surface chemisorption of oxygen OH^-. Therefore, the metal element M (M = Cr, Co and W) in the coating mostly exists in the form of M·OH and M·O in the corrosion products. With the increase in binding energy (BE), it is observed that the ratio of $[O^{2-}]/[O]$ increases and the ratio of $[OH^-]/[O]$ gradually decreases, indicating that the concentration of OH^- outside the corrosion product is higher than that inside.

The W4f high-resolution narrow spectrum of the corrosion products of two different solutions was fitted by peak value, and the peak values were around 32.06–35.6 and 34.23–37.5, respectively. These two peaks are representing the W4f 5/2 peaks of $W0^+$ from WC and $W6^+$ from WO_3. Referring to the related literature [34–36], based on the peak of W4f and O 1s, the corrosion product was determined as WO_3 and WC (Figure 12(c) and (d)). Picas et al. [37] studied the corrosion behavior of WC–Co–Cr coatings using HVOF in 25°C hydrochloric acid solution, and found corrosion products such as WO_3 and CoO/Co_3O_4. Compared with Figure 7(e), it can be seen through SEM that a large number of spherical WC particles exist, the results indicate that oxidation can hardly take place on the WC phase on the test surface at extreme cold conditions. While the W_2C peaks are not found in the

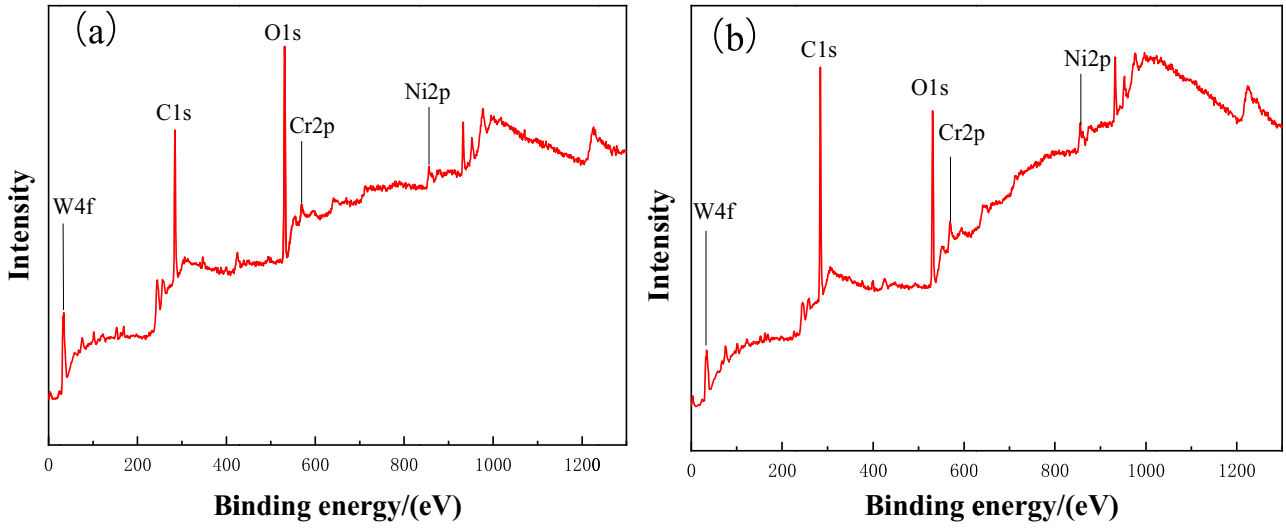

Figure 11: XPS full spectrum of sample surface after immersing in: (a) 3.5 wt% NaCl solution; (b) 0.5 mol·L^{-1} HCl solution.

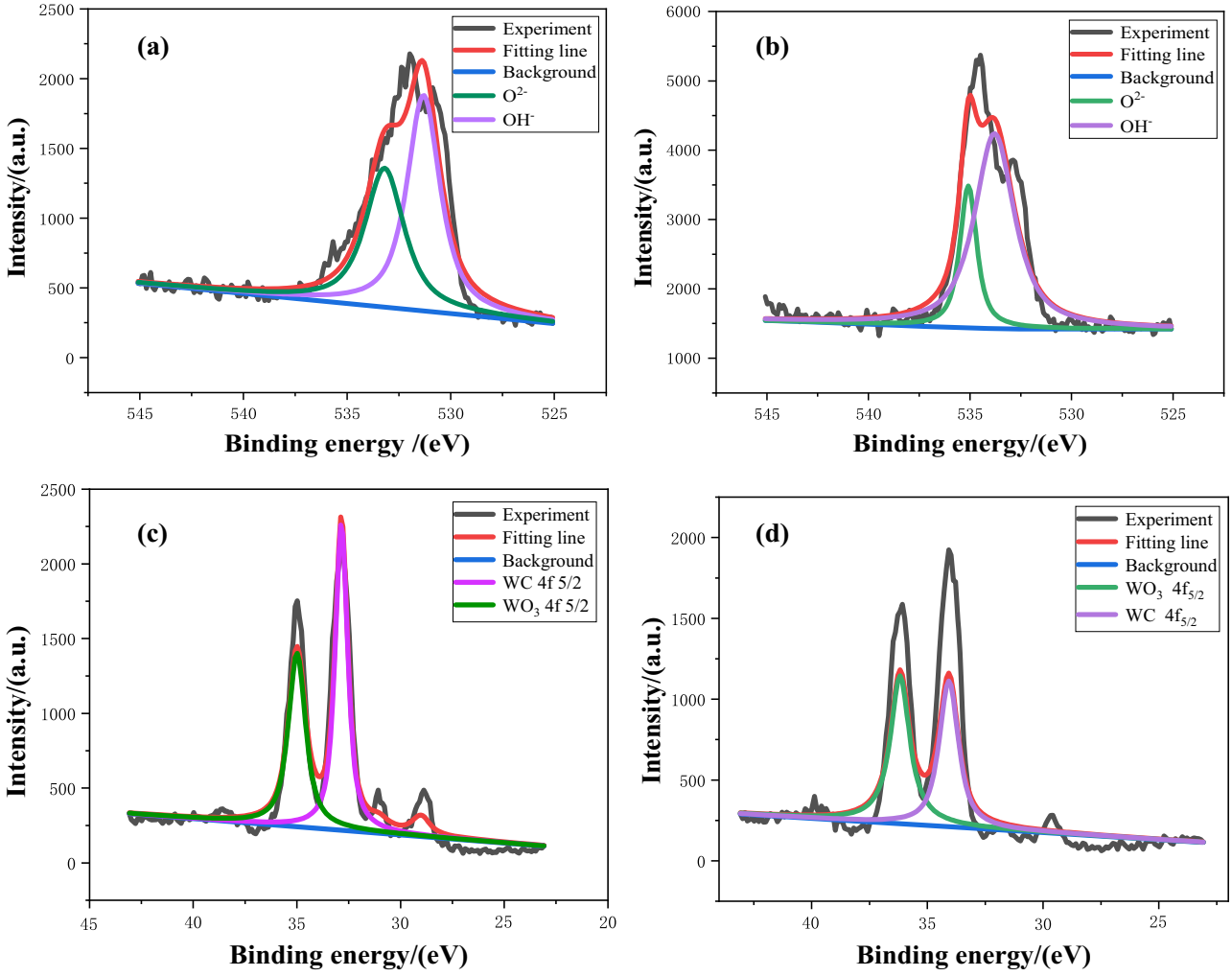

Figure 12: XPS spectra of the surface of Co + 45% WC sample after low temperature immersion. (a) O 1s in 3.5 wt% NaCl solution; (b) O 1s in 0.5 mol·L^{-1} HCl solution; (c) W4f in 3.5 wt% NaCl solution; (d) W4f in 0.5 mol·L^{-1} HCl solution.

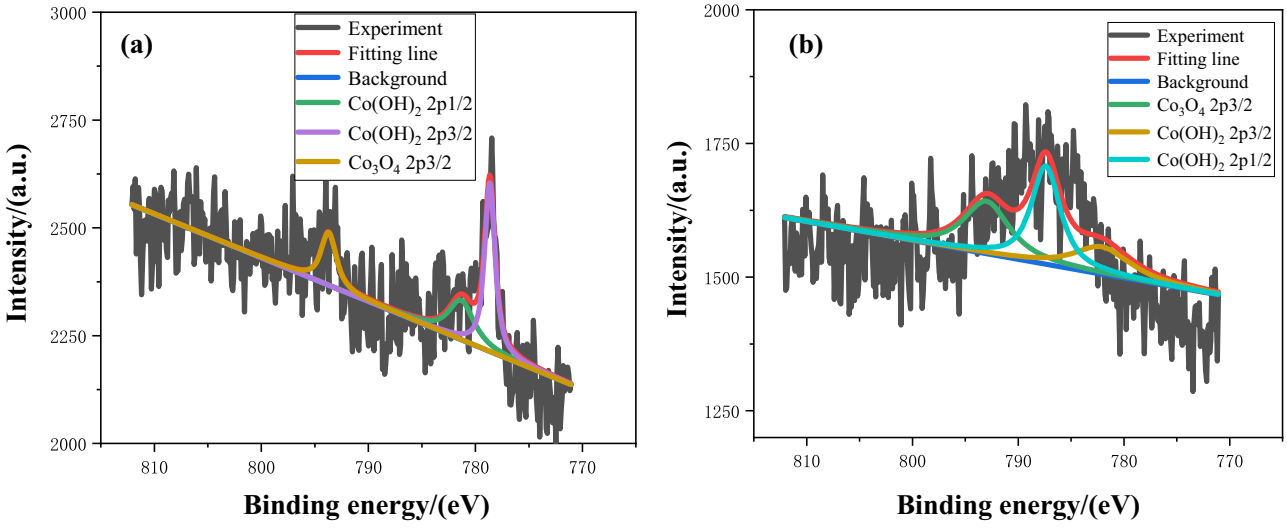

Figure 13: XPS spectra of the surface of Co-based sample after low temperature immersion. (a) Co 2p in 3.5 wt% NaCl solution; (b) Co 2p in 0.5 mol·L^{-1} HCl solution.

Figure 12(c) and (d), which is consistent with the previous XRD test results.

Figure 13(a) and (b) shows the XPS results of Co-based composite coating after immersed in 3.5 wt% NaCl and 0.5 mol·L^{-1} HCl solution at −40°C for 240 h, respectively. There are mainly three peaks, the BE of them is nearly 781, 788 and 795 eV, respectively. The former two peaks are representing the Co $2p_{3/2}$ and Co $2p_{1/2}$ peaks of Co^{2+} form $Co(OH)_2$. The peak at 795 eV represents the Co $2p_{3/2}$ peak of Cobalt oxide (Co^{2+}/Co^{3+}) form Co_3O_4. By combining the peaks of Co 2p and O 1s, the typical corrosion products are determined as $Co(OH)_2$ and Co_3O_4. It is reported that the corrosion process of Co-based cemented carbide is the reaction of dissolving cobalt on the anode into Co^{2+} and

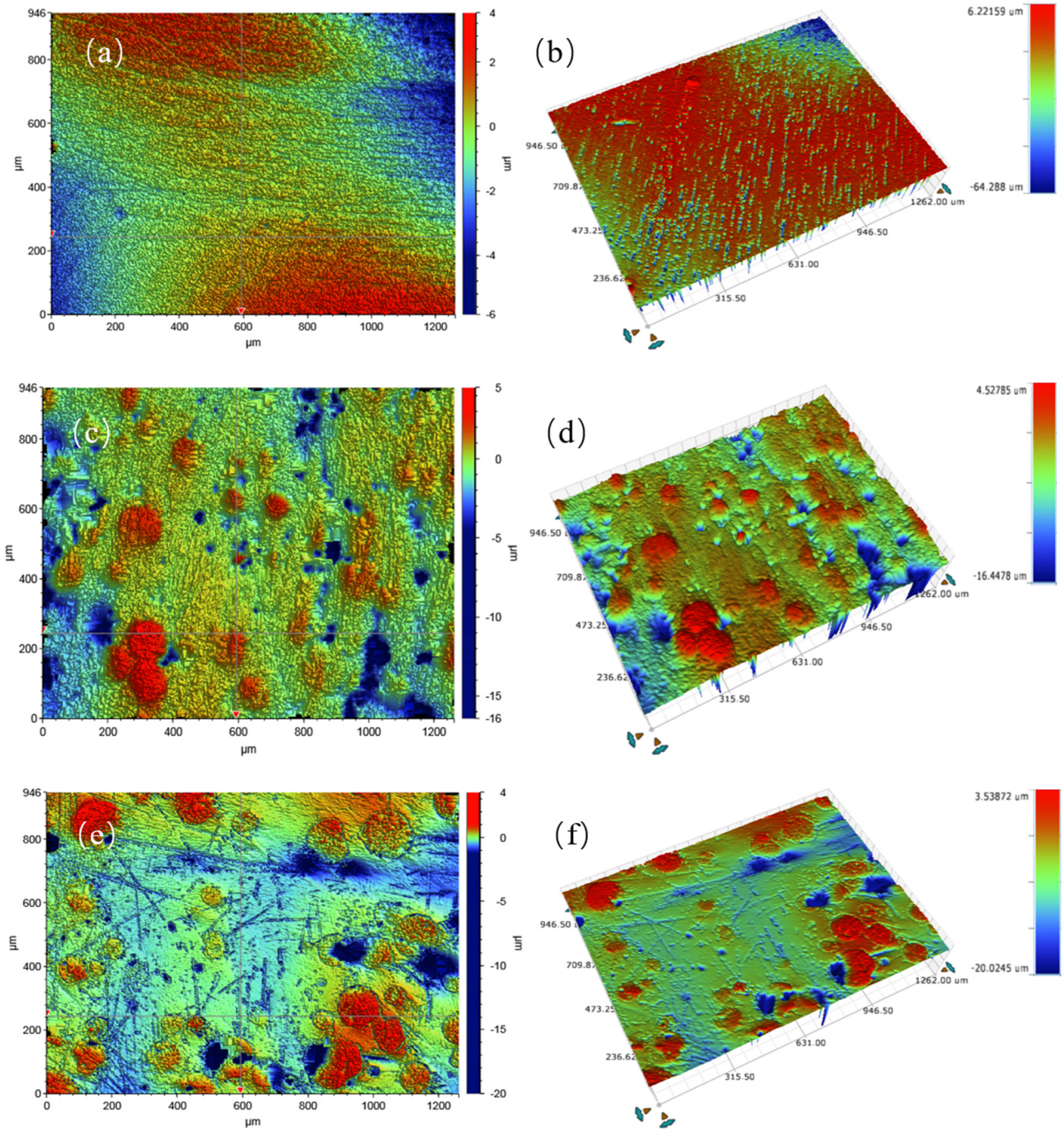

Figure 14: White light morphology after low temperature immersion corrosion. (a and b) Co coating in 3.5 wt% NaCl solution; (c and d) Co + 45% WC coating in 3.5 wt% NaCl solution; (e and f) Co + 60% WC coating in 3.5 wt% NaCl solution.

the reaction of the cathode being the oxidation reaction of H_2O and O^{2-} to OH^-, which also confirms that there is a large amount of OH^- in the outer layer. In addition, because the solubility of oxygen in water at -40°C is higher than that of ordinary room temperature, the oxidation-reduction reaction proceeds more strongly, the intensity of 2p3/2 peaks is higher (Figure 11(a)), and more corrosion product $Co(OH)_2$ is produced. Since the Co layer on the anode will react with H_2O to form CoO [38], and then continue to oxidize to form Co_3O_4, a large amount of H^+ ions and electrons will be generated during the reaction. However, there are more H^+ ions in 0.5 mol·L^{-1} HCl solution. According to the chemical equilibrium reaction, more number of H^+ ions will delay the formation of Co_3O_4. Therefore, in 3.5 wt% NaCl solution, the peak intensity of Co 2p3/2 is higher, and more Co_3O_4 corrosion products are generated than that in 0.5 mol·L^{-1} HCl solution [25].

3.5 3D surface topography of low temperature immersion corrosion

Through the white light diffraction experiment, we can see the 3D corrosion morphology of the composite coating after being immersed in an acidic solution at −40°C for 240 h, which demonstrates the variations in size and depth of the pits clearly [39]. By contrasting the optical profile results of the sample surface after corrosion. Therefore, the corrosion surface characteristics of WC–Co coating can be evaluated by observing and measuring the depth and density of the corrosion pits or corrosion surfaces. More pitting corrosion and deeper pits result in poor corrosion performance.

Figure 14(a) and (b) shows the optical profilometry (OP) results of the corroded surface of Co-based coating. The corrosion morphology of the sample is relatively uniform corrosion. Due to the existence of a large amount of Cl^- within a small radius and strong penetration ability, it is easy to be adsorbed near the uneven boundary and impurities. The surface is mainly locally dissolved and pitted to form micropores [40]. The interval of the concave part is between 0 and 2 μm, and the surface is very rough.

The cobalt based coating with spherical WC, as shown in Figure 14(c–f), we can see a large number of pitting pits. This morphology is consistent with the previous potentiodynamic polarization curve results in Figure 8. The addition of different amounts of WC particles will make the degree of corrosion and the depth of the corrosion pits different. This is because the coefficient of thermal expansion of the hard particles (WC/W_2C) are much different from that of the metal substrate, and the longitudinal and transverse thermal expansions of the coating. The different coefficients produce different thermal expansion and contraction, resulting in residual stress caused by nonuniform solidification. Pitting corrosion is easy to occur at the interface defects [41]. As shown in images, we can see a large number of pitting pits. The pitting holes of Co + 60% WC (average 10–12 μm) are significantly larger and deeper than those in Co + 30% WC, while the pitting depth of Co + 45% WC is about 8–10 μm. Therefore, through the analysis of surface morphology, it is concluded that Co + 45% WC has good corrosion resistance in low temperature environment.

4 Conclusion

Co-based alloy coatings with different amounts of WC were prepared on the surface of EH40 steel by PTA surfacing technology. The constituent phase, microstructure, corrosion resistance and corrosion products were analyzed. The following conclusions can be drawn:

(1) By observing the micro morphology of the PTA samples after etching, in addition to WC particles, solid solution γ-Co and FeNi were the major phases of the microscopic phase, Mo_2C, $MoNi_4$ and $Cr_2Fe_{14}C$ dispersed in the γ-(Ni, Fe) matrix. Because of the higher thermal reaction, for Co + 60% WC samples containing more WC particles, WC is easier to decompose into W_2C and C.
(2) Co + 45% WC and Co + 60% WC showed small spontaneous passivation interval in the polarization test after cryogenic treatment. A passivation film was formed by the metal on the coating surface. With the addition of WC, the coefficient of thermal expansion of the hard particles (WC/W_2C) is different from that of the Co coating. More WC leads to uneven solidification and residual stress. Pitting corrosion is easy to occur at the interface defects. Through experiment results, Co + 45% WC sample was determined to have a better corrosion resistance.
(3) The main corrosion products of cryogenic immersion were $Co(OH)_2$ and Co_3O_4, these corrosion products aggregate to form a stable corrosion product film, which plays some protective role for the coating. Hard particles WC are also partially oxidized to WO_3. The solubility of oxygen in water is higher at -40°C, the oxidation-reduction reaction proceeds more strongly, the corrosion product $Co(OH)_2$ has more.

Acknowledgements: The authors gratefully acknowledge the fund support of Shanghai Maritime University and Shanghai Jian Qiao University.

Funding information: The authors gratefully acknowledge the support of the Shanghai special fund (2019-jmrh1-kj45); Shanghai Engineering Technology Research Center of Deep Offshore Material (19DZ2253100), and Science & Technology Program of Shanghai Jian Qiao University (No.SJQ19012).

Author contributions: QiZheng Cao wrote the original draft and conducted the experiments, Li Fan revised and polished the draft, HaiYan Chen supervised and designed the experiments, YuRong Xu curated the experimental data and LiHua Dong contributed to the conception of the study.

Conflict of interest: Authors state no conflict of interest.

Data availability statement: The raw/processed data required to reproduce these findings cannot be shared at this time as the data also forms part of an ongoing study.

References

[1] Gautier, D. L., K. J. Bird, R. R. Charpentier, A. Grantz, D. W. Houseknecht, T. R. Klett, et al. Assessment of undiscovered oil and gas in the arctic. *Science*, Vol. 324, No. 5931, 2009, pp. 1175–1179.

[2] Topaj, A. G., O. V. Tarovik, A. A. Bakharev, and A. A. Kondratenko. Optimal ice routing of a ship with icebreaker assistance, *Applied Ocean Research*, Vol. 86, 2019, pp. 177–187.

[3] Zhang, J., O. Gaidai, K. M. Wang, J. H. Xu, R. C. Ye, and X. S. Xu. A stochastic method for the prediction of icebreaker bow extreme stresses. *Applied Ocean Research*, Vol. 87, 2019, pp. 95–101.

[4] Wang, K., L. Wu, Y. Z. Li, and C. Qin. Experimental study on low temperature fatigue performance of polar icebreaking ship steel. *Ocean Engineering*, Vol. 216, 2020, id. 107789.

[5] Shen, Y. Y., Y. H. Dong, H. D. Li, X. T. Chang, D. S. Wang, Q. H. Li, et al. The influence of low temperature on the corrosion of EH40 steel in a NaCl solution. *International Journal of Electrochemical Science*, Vol. 13, No. 7, 2018, pp. 6310–6326.

[6] Zhang, H. M., Y. Li, N. Li, L. Yan, Y. Y. Zhu, C. S. Wang, et al. The behaviour of tribocorrosion on EH47 high-strength ship hull steel in a 3.5% NaCl solution. *International Journal of Electrochemical Science*, Vol. 14, No. 12, 2019, pp. 11065–11080.

[7] Wei, X. Y., P. Jin, Y. P. Xia, H. M. Yu, W. B. Zhang, and Y. Cao. Corrosion behavior of WC–Co–(Ni)–(Cr) cemented carbide in neutral solution. *Xi You Jin Shu Cai Liao Yu Gong Cheng*, Vol. 49, No. 1, 2020, pp. 312–319.

[8] Wei, X. Y., P. Jin, Y. P. Xia, J. Z. Long, W. B. Zhang, T. Xu, et al. XPS and AES surface analysis of WC–Co–(Cr) cemented carbide after immersion in neutral solution. *Surface and Interface Analysis*, Vol. 52, No. 12, 2020, pp. 845–849.

[9] Scendo, M. and K. Szczerba. Influence of heat treatment on corrosion of mild steel coated with WC–Co–Al_2O_3 cermet composite produced by electrospark deposition. *International Journal of Electrochemical Science*, Vol. 14, No. 1, 2019, pp. 1009–1023.

[10] Wang, Q., L. X. Li, G. B. Yang, X. Q. Zhao, and Z. X. Ding. Influence of heat treatment on the microstructure and performance of high-velocity oxy-fuel sprayed WC–12Co coatings. *International Journal of Electrochemical Science*, Vol. 206, No. 19–20, 2012, pp. 4000–4010.

[11] Liu, Y., Z. Q. Hang, N. Y. Xi, H. Chen, C. P. Ma, and X. Y. Wu. Erosion-corrosion behavior of HVOF WC–Co coating in Cl^- and SO_4^{2-} containing solutions. *Applied Surface Science*, Vol. 431, No. 1, 2018, pp. 55–59.

[12] Kılıçay, K. and E. Kaya. Improvement of microstructural and tribological properties of APS carbide coatings via PTA surface melting. *International Journal of Food Engineering*, Vol. 98, No. 3, 2020, pp. 129–137.

[13] Cheng, Q., H. Y. Chen, Y. Hou, Y. R. Xu, L. Fan, and L. H. Dong. Microstructure and wear behavior of spherical NbC hardmetals with nickel-based binders on AISI 4145H steel. *International Journal of Refractory Metals & Hard Materials*, Vol. 95, 2021, id. 105414.

[14] Chao, M. J., X. Niu, B. Yuan, E. J. Liang, and D. S. Wang. Preparation and characterization of *in situ* synthesized B_4C particulate reinforced nickel composite coatings by laser cladding. *Surface and Coatings Technology*, Vol. 201, No. 3–4, 2006, pp. 1102–1108.

[15] Ding, X., D. Ke, C. Q. Yuan, Z. X. Ding, and X. D. Cheng. Microstructure and cavitation erosion resistance of HVOF deposited WC–Co coatings with different sized WC. *Coatings*, Vol. 8, No. 9, 2018, id. 307.

[16] Liu, A. J. and N. Liu. Effect of WC–Co granules on mechanical properties and microstructure of Ti (C, N)-based cermets. *Ceramics International*, Vol. 42, No. 14, 2016, pp. 15274–15284.

[17] Cui, C. Y., Z. X. Guo, Y. H. Liu, Q. Q. Xie, Z. Wang, J. D. Hu, et al. Characteristics of cobalt-based alloy coating on tool steel prepared by powder feeding laser cladding. *Optics & Laser Technology*, Vol. 39, No. 8, 2007, pp. 1544–1550.

[18] Hou, Y., H. Y. Chen, L. Fan, Y. R. Xu, Q. Cheng, and L. H. Dong. Corrosion behavior of cobalt alloy coating in NaCl solution. *Materials Science Forum*, Vol. 993, 2020, pp. 1086–1094.

[19] Yang, X. T., X. Q. Li, Q. B. Yang, H. L. Wei, X. Y. Fu, and W. S. Li. Effects of WC on microstructure and corrosion resistance of directional structure Ni60 coatings. *Surface and Coatings Technology*, Vol. 385, 2020, id. 125359.

[20] Shi, Y., X. D. Du, P. C. Zhuang, and H. Zhang. Effect of WC particles with different shapes during plasma spray on the properties of Fe-based composites coatings. *Materials Research Express*, Vol. 6, No. 11, 2019, id. 1165.

[21] Richter, J. and R. Michalik. Corrosion resistance of WC–Co and WC–Ni type sintered carbides in acetic acid water solution. *Corrosion Science*, Vol. 70, No. 1, 2019, pp. 128–134.

[22] Zhang, P. X., Y. B. Pang, and M. W. Yu. Effects of WC particle types on the microstructures and properties of WC-reinforced

Ni60 composite coatings produced by laser cladding. *Metals*, Vol. 9, No. 5, 2019, id. 583.

[23] Dong, Y. H., L. Fan, H. Y. Chen, L. H. Dong, Y. Y. Sheng, and F. H. Sun. Corrosion behavior of plasma transferred arc Fe-based coating reinforced by spherical tungsten carbide in hydrochloric acid solutions. *Journal of Wuhan University of Technology-Mater. Sci. Ed.*., Vol. 35, No. 2, 2020, pp. 299–309.

[24] Rocha, A. M. F., A. C. Bastos, J. P. Cardoso, F. Rodrigues, C. M. Fernandes, E. Soares, et al. Corrosion behaviour of WC hardmetals with nickel-based binders. *Corrosion Science*, Vol. 147, 2019, pp. 384–393.

[25] Fazili, A., M. R. Derakhshandeh, S. Nejadshamsi, L. Nikzad, M. Razavi, and E. Ghasali. Improved electrochemical and mechanical performance of WC–Co cemented carbide by replacing a part of Co with Al_2O_3, *Journal of Alloys and Compounds*, Vol. 823, 2020, id. 153857.

[26] Fan, B. W., S. G. Zhu, W. W. Dong, H. Ding, Y. F. Bai, Y. L. Luo, et al. Comparative study on corrosion behavior of WC-MgO composite and WC-6Co cemented carbide in NaCl solution. *Ceramics International*, Vol. 47, No. 5, 2021, pp. 7106–7116.

[27] Fan, H. B., W. Zheng, G. Y. Wang, P. K. Liaw, and J, Shen. Corrosion behavior of $Fe_{41}Co_7Cr_{15}Mo_{14}C_{15}B_6Y_2$ bulk metallic glass in sulfuric acid solutions. *Metallurgical and Materials Transactions A: Physical Metallurgy and Materials Science*, Vol. 42, No. 6, 2010, pp. 1524–1533.

[28] Han, B., W. W. Dong, B. W. Fan, and S. G. Zhu. Comparison on the immersion corrosion and electrochemical corrosion resistance of WC–Al_2O_3 composites and WC–Co cemented carbide in NaCl solution. *RSC Advances*, Vol. 11, No. 36, 2021, pp. 22495–22507.

[29] Hochstrasser-Kurz, S., Y. Mueller, C. Latkoczy, S. Virtanen, and P. Schmutz. Analytical characterization of the corrosion mechanisms of WC–Co by electrochemical methods and inductively coupled plasma mass spectroscopy. *Corrosion Science*, Vol. 49, No. 4, 2007, pp. 2002–2020.

[30] Wang, Y. F., G. X. Cheng, W. Wu, Q. Qiao, Y. Li, and X. F. Li. Effect of pH and chloride on the micro-mechanism of pitting corrosion for high strength pipeline steel in aerated NaCl solutions. *Applied Surface Science*, Vol. 349, 2015, pp. 746–756.

[31] Guo, S. D., W. Yan, J. H. Yi, S. L. Wang, X. Huang, S. R. Yang, et al. The optimization of mechanical property and corrosion resistance of WC-6Co cemented carbide by Mo_2C content. *Ceramics International*, Vol. 46, No. 11, 2020, pp. 17243–17251.

[32] Wei, L., Y. Liu, Q. Li, and Y. F. Cheng. Effect of roughness on general corrosion and pitting of (FeCoCrNi)0.89(WC)0.11 high-entropy alloy composite in 3.5 wt% NaCl solution. *Corrosion Science*, Vol. 146, 2019, pp. 44–57.

[33] Zou, D. N., R. Liu, J. Ll, W. Zhang, D. Wang, and Y. Han. Corrosion resistance and semiconducting properties of passive films formed on $00Cr_{13}Ni_5Mo_2$ supermartensitic stainless steel in Cl^- environment. *Journal of Iron and Steel Research International*, Vol. 21, No. 6, 2014, pp. 630–636.

[34] Chen, Z., M. L. Qin, P. Q. Chen, M. Huang, R. Li, S. J. Zhao, et al. WC-Co-Cr_3C_2-VC nanocomposite powders fabricated by solution combustion synthesis and carbothermal reduction. *Ceramics International*, Vol. 43, No. 12, 2017, pp. 9568–9572.

[35] Chen, L. Y., D. Q. Yi, B. Wang, H. Q. Liu, and C. P. Wu. Mechanism of the early stages of oxidation of WC–Co cemented carbides. *Corrosion Science*, Vol. 103, 2016, pp. 75–87.

[36] Zhang, X., J. H. Zhou, C. Liu, K. Li, W. J Shen, Z. Lin, et al. Effects of Ni addition on mechanical properties and corrosion behaviors of coarse-grained WC-10(Co, Ni) cemented carbides. *International Journal of Refractory Metals & Hard Materials*, Vol. 80, 2019, pp. 123–129.

[37] Picas, J. A, M. Punset, E. Ruperez, S. Menargues, E. Martin, and M. T. Baile. Corrosion mechanism of HVOF thermal sprayed WC–Co–Cr coatings in acidic chloride media. *Surface and Coatings Technology*, Vol. 371, 2019, pp. 378–388.

[38] Su, Q., S. G. Zhu, D. Hao, Y. F. Bai, and P. Di. Effect of the additive VC on tribological properties of WC-Al_2O_3 composites. *International Journal of Refractory Metals & Hard Materials*, Vol. 75, 2018, pp. 111–117.

[39] Katiyar, P. K. and N. S. Randhawa. Corrosion behavior of WC–Co tool bits in simulated (concrete, soil, and mine) solutions with and without chloride additions. *International Journal of Refractory Metals & Hard Materials*, Vol. 85, 2019, id. 105062.

[40] Fu, X. Q., W. K. Ma, S. L. Duan, Q. Q. Wang, and J. R. Lin. Electrochemical corrosion behavior of Ni-Fe-Co-P alloy coating containing nano-CeO_2 particles in NaCl solution. *Materials*, Vol. 12, No. 16, 2019, pp. 2614–2629.

[41] Tillmann, W., H. G. Lei, and W. F. Luo. Process parameter settings and their effect on residual stresses in WC/W_2C-reinforced iron-based arc sprayed coatings. *Coatings*, Vol. 7, No. 8, 2017, pp. 2079–6412.